DOI: 10.13009/EUCASS2019-1022

High-order large eddy simulation of particle-laden flow in a T106C low-pressure turbine linear cascade

Patrick Kopper[⋆]*, Andrea Beck*[†]*, Philip Ortwein*[†]*, Nico Krais*[†]*, Daniel Kempf*[†]*, Christian Koch*[⋆]
[⋆]*Institute of Aircraft Propulsion Systems, University of Stuttgart*
Pfaffenwaldring 6, 70569 Stuttgart, Germany
[†]*Institute of Aerodynamics and Gas Dynamics, University of Stuttgart*
Pfaffenwaldring 21, 70569 Stuttgart, Germany
patrick.kopper@ila.uni-stuttgart.de · andrea.beck@iag.uni-stuttgart.de · philip.ortwein@iag.uni-stuttgart.de ·
nico.krais@iag.uni-stuttgart.de · daniel.kempf@iag.uni-stuttgart.de · christian.koch@ila.uni-stuttgart.de

Abstract

Erosion and fouling of engine blades and subsequent performance degradation due to particle-laden flows pose a complex multiscale and multiphysics problem for CFD simulation. This work presents a framework for turbomachinery simulations which predicts particle motion on a time-accurate LES flow field obtained with high-order accurate Discontinuous Galerkin Spectral Element Method (DGSEM). As a first application of this framework, the particle-laden flow in a T106C subsonic low-pressure turbine cascade is shown. Potential benefits of time-accurate LES compared to RANS are outlined and the dependence of particle-laden LES on accurate inflow conditions is highlighted.

1. Introduction

Aircraft engine manufacturers strive for continuously improved fuel efficiency, driven by consumer and environmentally regulatory demands. Therefore, the focus is shifted from initial performance evaluation towards continuous life cycle monitoring and prediction. Airborne particles either ingested from the environment or created during engine operation continuously remove host material from engine blades (erosion) or cause unwanted deposition (fouling). Both cases result in engine performance degradation and eventually require maintenance. The current state of the art approach for the numerical prediction of erosion and fouling relies on a segregated procedure: first a time-averaged flow solution is obtained using Reynolds-Averaged Navier-Stokes (RANS) methods, then particle trajectories are computed a posteriori on this flow field. Macroscopic, integral effects such as erosion and fouling are subsequently extrapolated from impact statistics and empirical correlations while the resulting changes in blade geometry are usually neglected or evaluated at discrete steps. However, the separation of these inherently coupled processes into sequential steps in a feed-forward manner results in the loss of higher order statistics at each stage which must be reconstructed using additional models and assumptions. These assumptions clearly rely on the accuracy of the RANS solution which is problematic in typical turbomachinery applications, including cases with large scale unsteadiness[1]. The inherent uncertainties, often coupled with the use of closed-source software, results in a wide spread of results, sometimes even within different release versions of the same software package[2–5]. This work presents as an alternative a coupled particle tracking framework which is added to the existing high-order framework FLEXI for DNS and LES*, i.e. particles are tracked in a time-accurate manner on an unsteady solution and following the same time step. Our first goal is to investigate the effects of unsteady flow behavior on the particle motion by comparison against stationary flow fields within the same setup and framework. By quantifying these effects, we can highlight characteristics and challenges for the development of particle dispersion models.

This paper shows the application of this framework to the particle-laden flow through a T106C subsonic low-pressure high-load turbine blade arranged in a linear cascade. We briefly explain the physical models and their implementation in Section 2, followed by a description of our setup in Section 3. We validate the flow field results against literature data in Section 4. The main focus of this work is in Section 5 where we show and discuss particle behavior in specific regions of interest. We close with our conclusion and outlook in Section 6.

*www.flexi-project.org

DOI: 10.13009/EUCASS2019-1022

2. Governing Equations and Numerical Methods

2.1 Fluid Phase

The temporal and spatial evolution of a compressible Newtonian fluid with density ρ, velocity components u_i, specific total energy e and constant dynamic viscosity μ is prescribed by the Navier-Stokes-Fourier equations as

$$\begin{aligned} \frac{\partial \rho}{\partial t} + \frac{\partial \left(\rho u_j\right)}{\partial x_j} &= 0, \\ \frac{\partial \left(\rho u_i\right)}{\partial t} + \frac{\partial \left(\rho u_i u_j + p\delta_{ij}\right)}{\partial x_j} &= \frac{\partial \sigma_{ij}}{\partial x_j}, \\ \frac{\partial \left(\rho e\right)}{\partial t} + \frac{\partial \left[\left(\rho e + p\right) u_j\right]}{\partial x_j} &= -\frac{\partial q_j}{\partial x_j} + \frac{\partial \left(\sigma_{ij} u_i\right)}{\partial x_j}. \end{aligned} \tag{1}$$

The system is closed with the equation of a perfect gas $p = \rho RT$ where p is the pressure, T the temperature and R the universal gas constant. The viscous stress tensor σ_{ij} is defined as

$$\sigma_{ij} = \mu S_{ij}, \tag{2}$$

with the rate of strain tensor S_{ij} given by

$$S_{ij} = \frac{\partial u_i}{\partial x_j} + \frac{\partial u_j}{\partial x_i} - \lambda \delta_{ij} \frac{\partial u_k}{\partial x_k}. \tag{3}$$

As is common, the trace of S_{ij} is removed by assuming Stoke's hypothesis and choosing the bulk viscosity coefficient λ as $\frac{2}{3}$. The heat flux vector in Eq. (1) is modeled using Fourier's law, so

$$q_j = -k \frac{\partial T}{\partial x_j}, \quad \text{with } k = \frac{c_p \mu}{Pr}, \tag{4}$$

where Pr denotes the fluid's Prandtl number, c_p the specific heat and k is its thermal conductivity.

The fluid phase is discretized in the Eulerian framework with the Discontinuous Galerkin Spectral Element Method (DGSEM). The DGSEM in this framework is derived by obtaining the L_2 projection of Eq. (1) in vectorial form onto a space of polynomial test functions in a domain element Q, so the equation is rewritten as

$$\vec{U}_t + \vec{\nabla} \cdot \vec{\mathcal{F}}(\vec{U}, \vec{\nabla}\vec{U}) = 0, \tag{5}$$

where $\mathcal{F}$ denotes the flux vector. Projecting Eq. (5) onto the test funtion $\phi(\vec{x})$ and spacial integration by parts yields the weak DG formulation as

$$\frac{\partial}{\partial t} \int_Q \vec{U} \phi \, d\vec{x} + \oint_{\partial Q} \vec{\mathcal{F}} \phi \, d\vec{s} - \int_Q \vec{\mathcal{F}} \cdot \vec{\nabla} \phi \, d\vec{x} = 0. \tag{6}$$

The solution is approximated by a tensor product of 1D Lagrange polynomials. Using the collocation approach, we choose the interpolation and integration points identically as Gauss-(Lobatto-)Legendre quadrature points, integrate by Legendre-Gauss quadrature in space and advance in time using the fourth-order explicit Runge-Kutta method by Carpenter and Kennedy [6]. More details on this approach are given in Beck et al. [7].

2.2 Particle Phase

The particle phase is discretized in the Lagrangian framework since we are interested in the behavior of individual particles constituting a minuscule fraction of the total volume. Following Murrone and Villedieu [8], the total force on a particle imposed by the surrounding fluid is

$$m_p \frac{d\vec{u}_p}{dt} = \vec{F}_D + m_p \vec{g} + \vec{F}_L + \rho_f C_m \frac{\pi d^3}{6} \left(\frac{D\vec{u}_f}{Dt} - \frac{d\vec{u}_p}{dt} \right) - \rho_f \frac{\pi d_p^3}{6} \nabla p + \vec{F}_B, \tag{7}$$

with the subscript f denoting the local fluid quantities at the particle center and the subscript p the respective particle properties. m_p and d_p represent the particle mass and diameter, $\vec{F}_L$ the lift force and $\vec{F}_B$ the Basset force. Rudinger [9]

DOI: 10.13009/EUCASS2019-1022

showed all terms except the first two, namely the drag force $\vec{F}_D$ and the gravitational force, to be negligible for particles with density ratios $\rho_p/\rho_f \geq 10^3$. In this work, the drag is modeled with the model by Vinkovic et al. [10] which is based on the earlier model by Wang and Squires [11]. Using the mass-point approach and the kinematic viscosity ν, the particle Reynolds number Re_P is defined as

$$Re_p = \frac{\left|\vec{u}_p - \vec{u}_f\right| d_p}{\nu} \tag{8}$$

and the relaxation time τ_p is obtained by using the same quantities, so

$$\tau_p = \frac{\rho_p d_p^2}{18\rho_f \nu}. \tag{9}$$

For particle Reynolds numbers less than unity, the drag function $f(Re_p)$ must follow Stokes' law [12,13]. For higher Re_p, an empirical correction from Clift et al. [14] is employed,

$$f(Re_p) = \begin{cases} 1 & \text{if } Re_p < 1 \\ 1 + 0.15 Re_p^{0.687} & \text{otherwise.} \end{cases} \tag{10}$$

With this correction, the drag experienced by a single particle is prescribed as

$$\vec{F}_D\left(\vec{u}_f, \vec{u}_p\right) = m_p \frac{\vec{u}_f - \vec{u}_p}{\tau_p} f(Re_p). \tag{11}$$

Due to its magnitude and the high speed flow, the gravitational force is deemed irrelevant for the current work and thus not taken into account. The particle trajectories are obtained by evaluating Eq. (7) after interpolating the DGSEM field solution to the particle's center of mass and integrating the ODE in time coupled with the fluid phase using the same Runge-Kutta method. Boundary interactions are implemented using ray-tracing by detecting the intersection of the particle's trajectory $\vec{t} = \vec{x}^{new} - \vec{x}^{old}$ with the boundary face and enforced accordingly. A more detailed description of the used procedure including applications and verifications is given by Ortwein et al. [15].

3. Test Case Setup

The T106C subsonic low-pressure turbine linear cascade was chosen as test case for its extensive coverage in literature and the flow undergoing many typical regimes commonly expected in turbomachinery applications while passing the cascade [16,17]. In the current setup, the cascade operates at an isentropic exit Mach number of $Ma_{is} = 0.65$, with geometry and boundary conditions comprehensively described by Hillewaert et al. [18]. The high blade turning causes laminar-turbulent transition and eventually flow separation on the suction side due to the strong adverse pressure gradient in this area. The test case is set up using the physical chord length $c = 0.009\,301$ m resulting in an isentropic expansion Reynolds number of $Re_{is} = 80\,000$ with the domain extended approximately $2c$ axially upstream, $3c$ axially downstream of the blade and $0.1c$ in the z-direction. The mesh with 5311 elements in the x-y-plane is shown in Fig. 1. Pitchwise and spanwise boundaries are set as periodic and the polynomial degree of the ansatz for the DGSEM is chosen as 5. Simulations are performed in FLEXI as RANS with the Spalart-Allmaras turbulence model [19] and as implicit LES [7,20]. Additionally, the time-accurate LES was averaged spanwise and temporal direction in a post-processing step. The resulting flow field is considered to represent a theoretical ideal RANS solution.

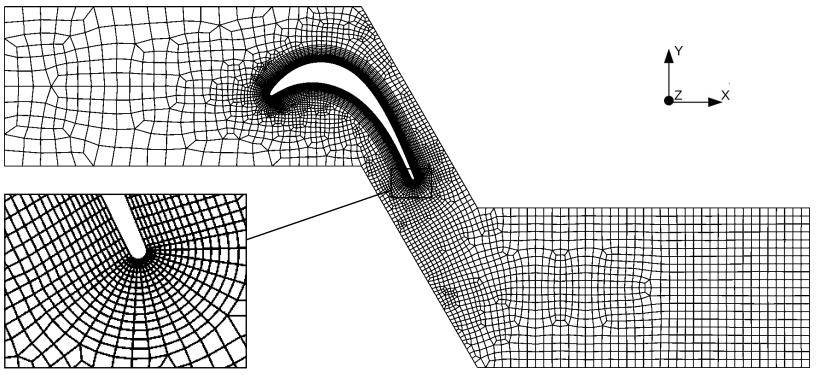

Figure 1: Mesh in the *x-y* plane with a zoom on the trailing edge region.

DOI: 10.13009/EUCASS2019-1022

Following the mass-point model outlined in Section 2.2, particles are modeled as smooth spheres of Arizona test dust medium with density $\rho_p = 1025\,\mathrm{kg/m^3}$, defined by ISO 12103-1:2016(E)[21]. The continuous distribution is split into 11 discrete species representing the lighter 83.5 percentile of the volume of the mixture and covering a Stokes number range from 0.0034 to 7.0146. The split into discrete species instead of a continuous function allows separate analysis for different behavioral regimes depending on the Stokes number. Particles are emitted randomly over the inlet boundary with velocity magnitude and direction equal to the mean free stream conditions. Periodic boundary conditions are enfored identical to the fluid phase and the particles are removed from the domain at the outlet. Furthermore, particles comply with a perfect reflection condition upon impact on the blade. Particle simulations are performed a posteriori on the stationary RANS and time-averaged LES field as well as coupled to the fluid solution in the time-accurate LES case. To determine the influence of upstream turbulence, all computations are repeated with the initial particle velocity superimposed with a Gaussian normal distribution with zero mean and 4% $|\vec{u}|_2$ standard deviation, independently drawn in all three coordinate directions.

All simulations are performed on the Cray XC40 "Hazel Hen" system at the High-Performance Computing Center (HLRS) Stuttgart. For the a posteriori simulations, the particle time step is selected comparable to the average LES time step while the time-accurate LES time step for both fluid and particle phase is determined using the CFL condition of the current solution.

4. Flow Field Results

Fig. 2 shows the Mach number distributions at the spanwise centerline in the RANS and time-accurate LES case. Apart from sporadic acoustic disturbances traveling upstream in the LES case, the flow fields are in good agreement prior to the blade's leading edge and on the pressure side. On the suction side, the RANS predicts an attached flow resulting in a narrow wake while the LES reveals a separating flow with the vortex-shedding behavior causing a widened, unsteady wake.

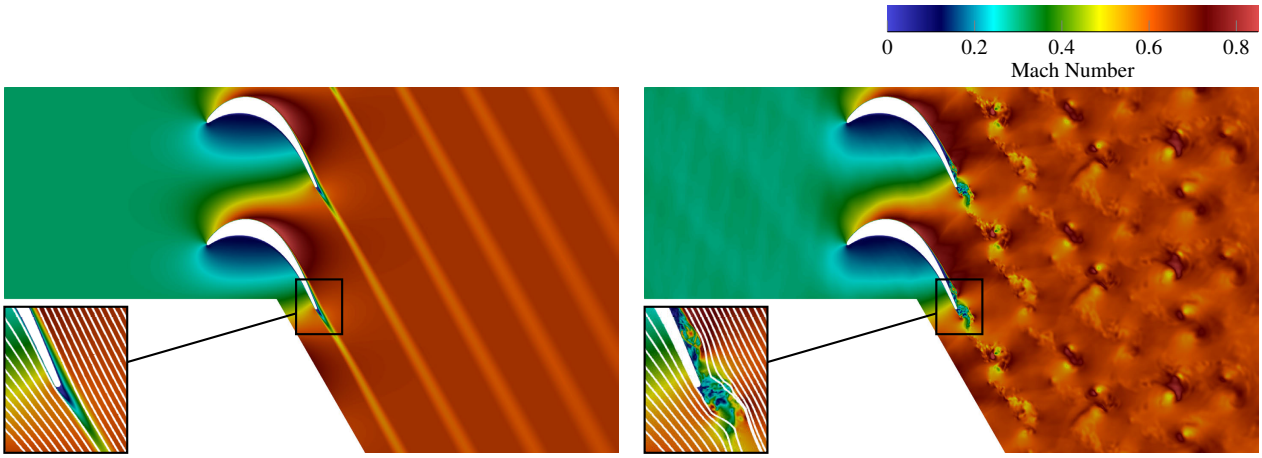

(a) RANS (b) LES

Figure 2: Mach number distribution at the spanwise centerline

Comparisons of isentropic Mach number M_{is} and skin friction coefficient C_f distributions over position on the axial chord x/C_x of the current simulations against results by Marty[16], de Wiart and Hillewaert[22] and Hillewaert and Galbraith[17] are given in Figs. 3a and 3b, respectively. In both cases, the current results show good agreement with the published results, even though the present RANS invokes the simpler one-equation Spalart-Allmaras model instead of the more advanced k-ω shear-stress transport (SST) model used by Marty[16]. All LES results indicate the separation point at 68% C_x while the RANS predicts a fully attached flow, matching the observations from Fig. 2.

5. Particle Phase Results

Interactions of particles with sampling surfaces on the blade surface and across the outlet are tracked in two separate ways. For the first approach, each sampling surface grid face is supersampled 4 times. The number of impacts as well as mean, min/max and standard deviation of particle kinetic energy upon impact and impact angle is evaluated using Welford's method, making integral data available at each time step[23]. In addition, the velocity vector, the impact angle

DOI: 10.13009/EUCASS2019-1022

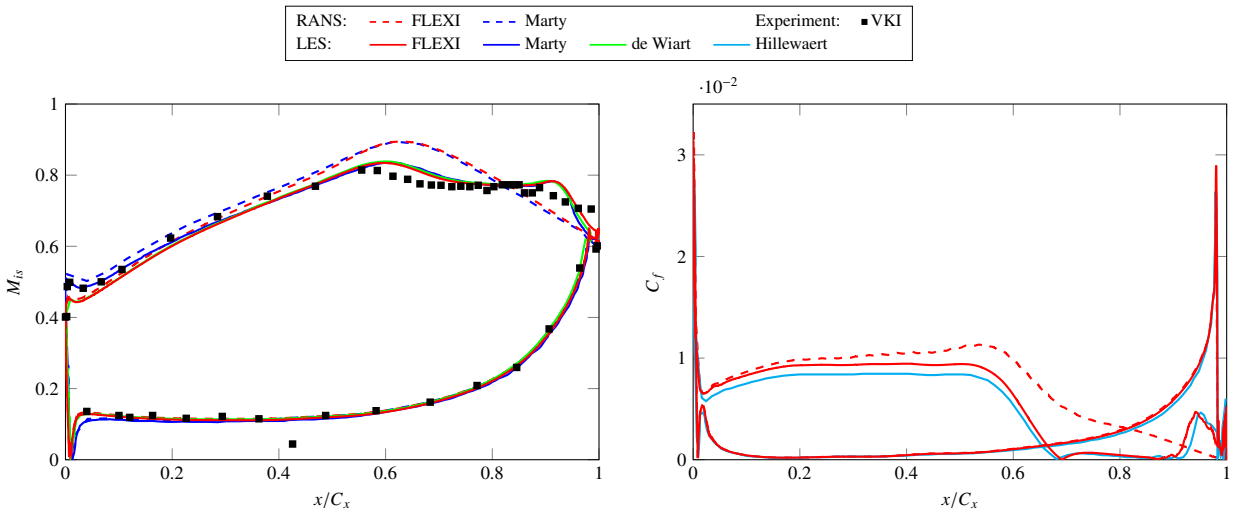

(a) Isentropic Mach number distribution

(b) Skin friction coefficient distribution

Figure 3: Comparison of isentropic Mach number M_{is} and skin friction coefficient C_f distributions over position on the axial chord x/C_x against results from Marty [16], de Wiart and Hillewaert [22] as well as Hillewaert and Galbraith [17]. Numerical results are denoted by lines. Experimental results by the Von Karman Institute (VKI) are published in Marty [16] and indicated by squares [1].

and the number of previous reflections is tracked for each individual particle along with the physical impact location in a grid independent way. A snapshot of individual particle trajectories together with average impact angle on the sampling surfaces in relation to the complete extension of the physical blade is given in Fig. 4.

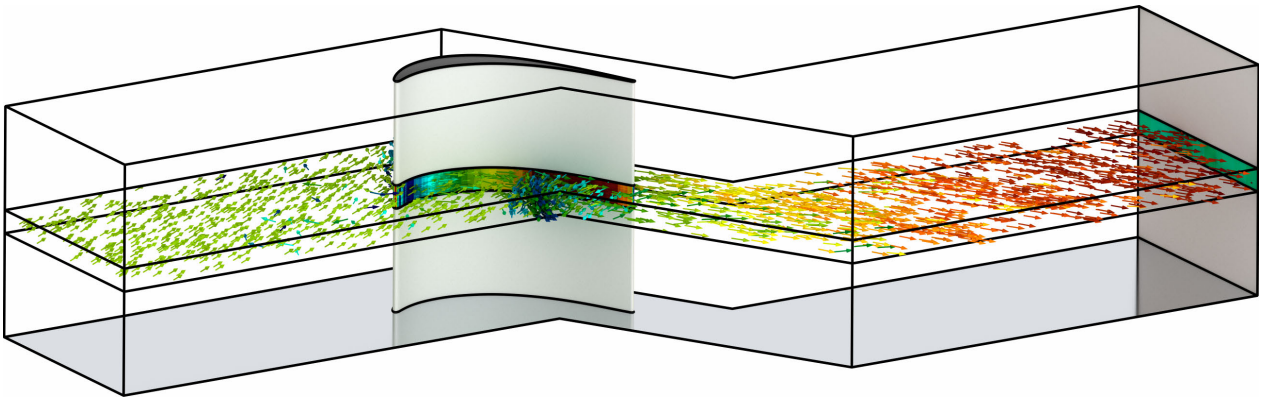

Figure 4: Simulated blade section in relation to a blade of $1c$ span, instantaneous trajectories of 44 µm particles and average impact angle on sampling surfaces.

5.1 General Particle Behavior

Fig. 5a visualizes the particle behavior in the RANS without initial random velocity component in the vicinity of the blade, with boxes emphasizing regions of interest. The homogeneously emitted particles approach the blade from the left in alignment with the flow field and exit at the right. For the following discussion, the Stokes number range can be categorized into three regimes. Particles with a Stokes number substantially lower than one act as nearly ideal tracers. As such, they rarely show interaction with solid geometry but react strongly to turbulent dispersion in the free stream. Particles with a Stokes number significantly higher than uniform behave almost ballistic. Their trajectory is mainly influenced by blade impacts and reflections, the accurate modeling of the latter one still being a challenge in the CFD community. Particles in between these two regimes react to the flow in a significant way but are still heavy enough to retain their particle characteristics without being reduced to mere tracers. Of course, these regimes are smoothly blended and visible in Fig. 5a at the same time.

DOI: 10.13009/EUCASS2019-1022

Upstream of the leading edge of the blade (region A), the light particles experience acceleration/deceleration through the flow field, which is adjusting to the blade curvature. We can also observe some particles impacting on the leading edge and being reflected back into the oncoming flow. Further downstream on the pressure side (region B), the heavier particles impact at nearly 90°, are reflected back and travel a short distance upstream while being slowed down by the incoming flow. They then revert their direction of travel and are convected downstream again with the main flow. Here, two particle families can be identified: The heavier sized particles have been accelerated along the suction side leading edge, but cannot follow the field further around the curvature due to inertia. Thus, they "separate" from the flow field in this region and travel along a free path (yellow colors). Lighter particles are able to manage the change in direction with the flow field and are constantly accelerated by it, reaching higher velocities and travel parallel to the blade (red colors). Region C highlights an interesting region in the boundary layer where the particle stream reflected from the above blade hits the aft surface of the considered blade. Fig. 5b provides a visual impression of the different particle behavior for the 22 µm species in this area. It shows the impact positions for individual particles on the last 30% of the blade chord for RANS (red) and time-accurate LES (blue) without initial turbulent contribution. A prominent feature is the sharp delimitation of impacts in upstream direction for the RANS computation while results for time-accurate LES are more scattered and cover a larger area than the RANS impacts. Region D focuses on the wake. Here, a region with lower particle numbers directly downstream of the trailing edge is identifiable, this can be attributed to the shielding by the blade. The heavier particles appear to be concentrated in rather narrow particle streams, while the lighter particles show greater spatial dispersion.

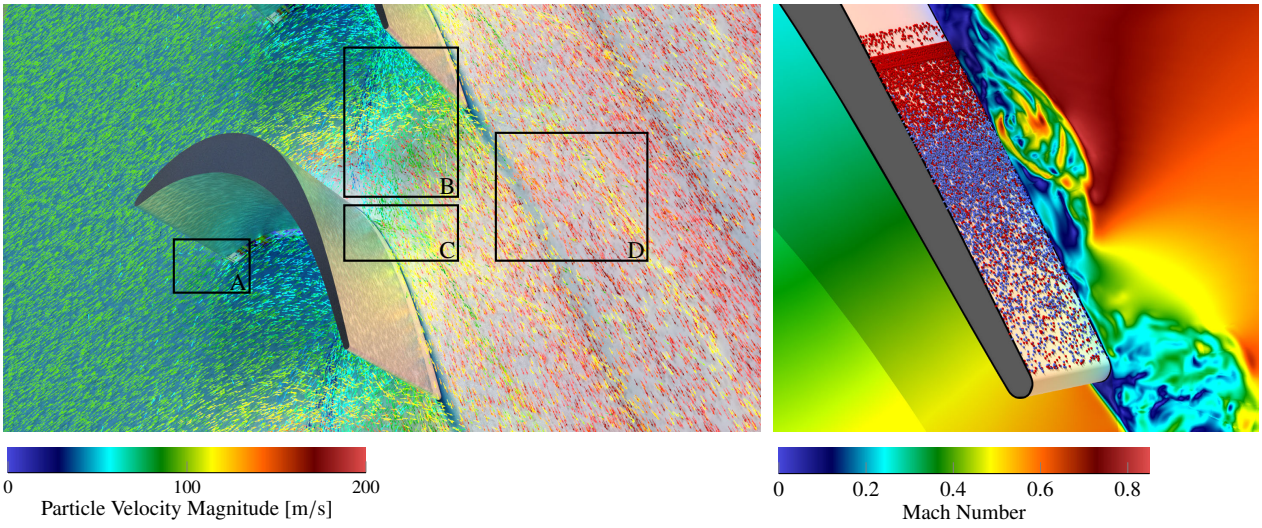

(a) Instantaneous particle phase in the blade vincinity

(b) Impact locations at the trailing edge

Figure 5: Visualization of instantaneous particle phase in the blade vicinity by their velocity vector at each particle position with data from RANS as well as impact locations for 22 µm particles at the trailing edge. In Fig. 5b, red color indicates RANS results and blue color corresponds to time-accurate LES. All simulations performed without initial random velocity component.

5.2 Characteristics of Particle Impacts on the Blade

Now turning to a quantitative analysis, we focus on particle species of 22 µm and 44 µm diameter, corresponding to Stokes numbers of 1.7536 and 7.0146. Both species are within the range where particles are influenced by the flow, but still retain their inertial characteristics. Fig. 6 gives the number of impacts along the blade chord position in percent of emitted particles with a bin width of 1% C_x. The graphs are further split into simulations without initial random velocity component (light solid lines) and simulations with an initial random velocity component of magnitude 4% $|\vec{u}|_2$ (dark dashed lines). It becomes immediately apparent in Figs. 6a and 6b that the non-uniform initial condition has only minor effects on the lighter species. Clearly, since all simulations feature a laminar flow field in the extent of $2c$ from the inlet location to the leading edge, this distance is sufficient to substantially reduce any contribution from the turbulent inlet condition for this Stokes number. Therefore, the pressure side where particles impact the blade over the whole remains virtually unchanged between all simulations. Only reflected particles hitting the suction side's trailing edge in Fig. 6b show some smearing effect. Furthermore, a slight forward shift of the impact locations is noticeable in

DOI: 10.13009/EUCASS2019-1022

the RANS case, a direct consequence of the missing separation outlined earlier. Heavier particles in Figs. 6c and 6d retain their particle characteristics much longer. As such, while the overall number of impacts remains unchanged regardless of the inlet boundary condition, the particles show significant smearing of formerly sharp spikes in impact numbers with a turbulent inlet condition, thereby also obscuring slight differences between the RANS and LES cases. Overall, we can note that an initial random component acts as a smooth filter with the effect growing more pronounced with increasing particle Stokes number.

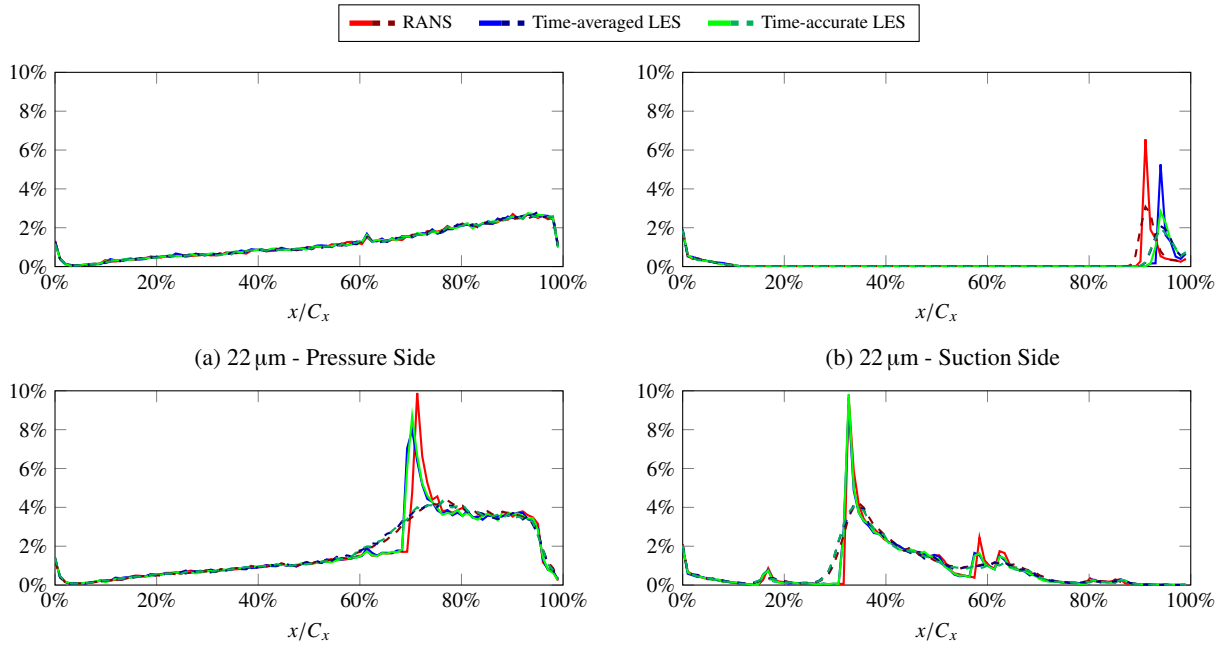

(a) 22 µm - Pressure Side

(b) 22 µm - Suction Side

(c) 44 µm - Pressure Side

(d) 44 µm - Suction Side

Figure 6: Percentage of emitted particles of a given size impacting on the blade per percent chord plotted over dimensionless axial chordwise position. Light solid lines denote the cases without particle inflow turbulence, dark dashed lines correspond to an initial random velocity component of magnitude 4% $|\vec{u}|_2$.

Erosion and fouling are strongly nonlinear processes, dependent not only on absolute number of particle impacts, but also on impact kinetic energy and angle. For these statistics, all simulations are in good agreement for the pressure side due to the laminar inflow condition and negligible effect of the difference between RANS and LES. The latter is important on the suction side, especially as particles pass through the separation region. Fig. 7 shows the spanwise averaged impact kinetic energy on the suction side for 22 µm and 44 µm particles. Focusing on the aft region in Fig. 7a, the lack of separation in the RANS leads to an almost constant impact kinetic energy in this simulation. Simulations resolving the flow separation feature decreasing kinetic energy towards the trailing edge as particles undergo deceleration while passing through the separation region. This deceleration is increasing in magnitude with longer residence time in the region, corresponding with impacts further downstream. Time-accurate LES shows an impact region expanded slightly upstream, a direct effect of the turbulent particle dispersion. While an initial random velocity component gives similar effects in the former two cases, this particle inflow condition has only a minor effect on the time-accurate LES.

More revealing than the mean values are histograms and kernel density estimations for particle kinetic energy upon impact on the blade trailing edge for 22 µm particles (compare aft region in Fig. 6b), shown in Figs. 8a and 8b for simulations without initial random velocity component and with initial random velocity component 4% $|\vec{u}|_2$, respectively. We selected this area as it embodies a clearly defined region and highlights effects of differing flow solutions. Overall, both plots give similar particle characteristics. Particles in RANS experience only minor deceleration in the boundary layer due to the lack of a separation bubble and have the highest kinetic energy. The energy range is narrow and nearly symmetrical, resembling a Gaussian distribution. Particles in the time-averaged LES pass the stationary separation bubble in this region, resulting in lower overall kinetic energy. Furthermore, a left handed skewness is introduced as longer residence time in the bubble results in stronger deceleration, but is also linked to a shallower impact angle. Thus, the number of impacting particles is decreasing as the blade additionally turns away from the mean flow direction. The time-accurate LES shows the broadest range of kinetic energy with pronounced skewness. Interestingly, while the average impact kinetic energy is identical between time-averaged and time-accurate LES, the maximum of the latter is shifted towards higher values. This plot outlines the challenges associated with reconstruction approaches

DOI: 10.13009/EUCASS2019-1022

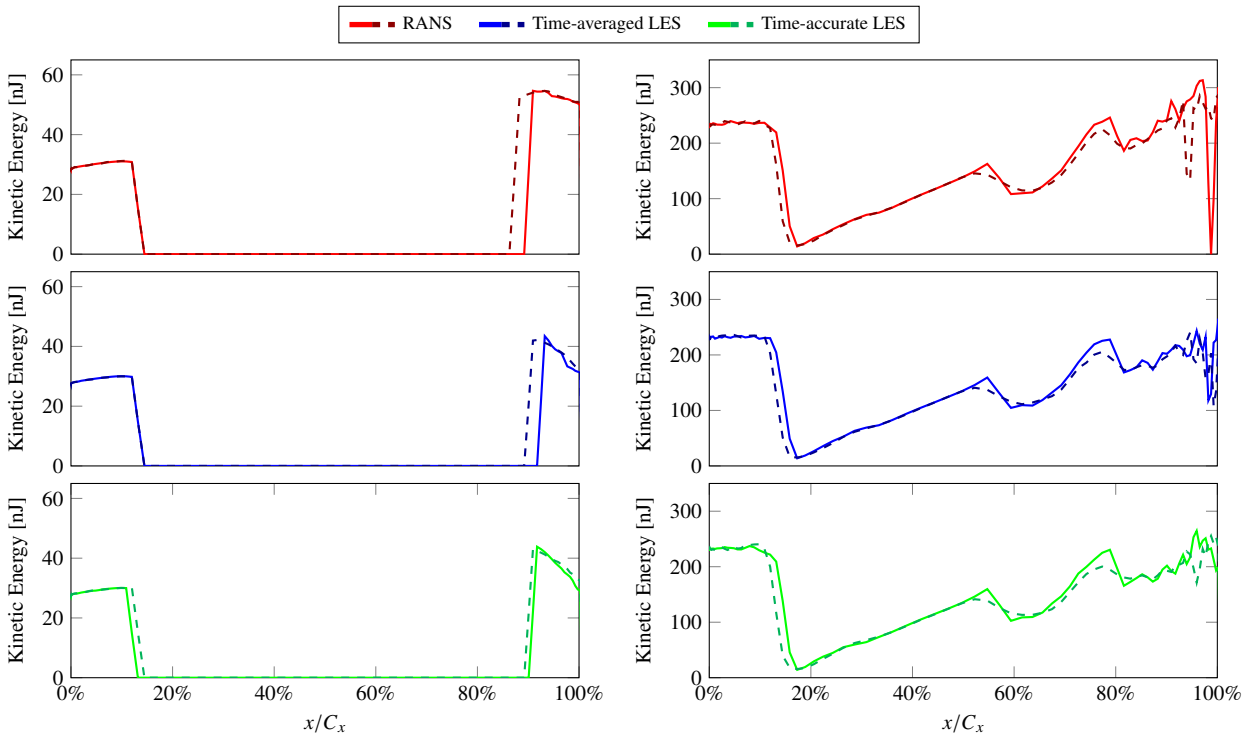

(a) 22 µm particles

(b) 44 µm particles

Figure 7: Averaged impact kinetic energy per surface grid element on the suction side for 22 µm and 44 µm particles. Light solid lines denote the cases without particle inflow turbulence, dark dashed lines correspond to an initial random velocity component of magnitude 4% $|\vec{u}|_2$.

for erosion modeling as higher particle statistics are strongly nonlinear and highly dependent on the underlying flow field. Focusing on differences between the simulations with and without initial random velocity component, we again notice some smearing of the results but not significantly enough to change the overall characteristics. We also want to point out that while the results in Fig. 8b look better converged, this does not necessarily need to be the case as detail D in Fig. 5a pointed out that a sharp delimitation of impacts occurs in the RANS and some spikes in the energy statistics can be expected.

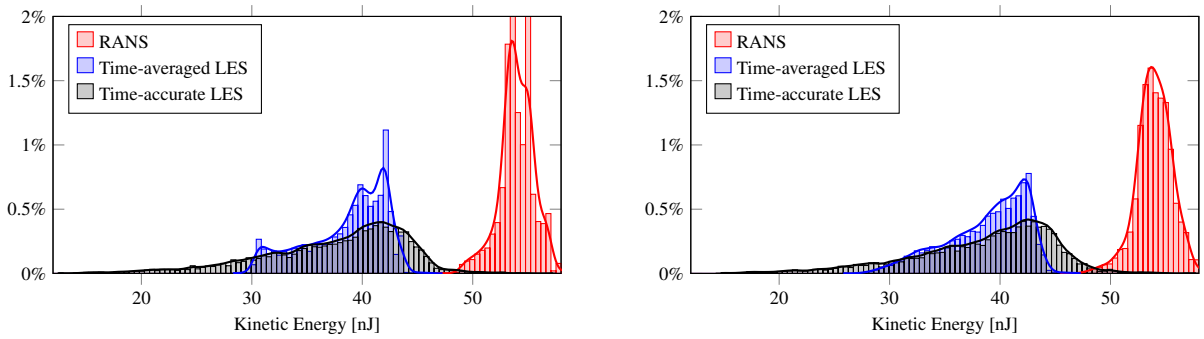

(a) Without initial random velocity component

(b) Initial random velocity component 4% $|\vec{u}|_2$

Figure 8: Histograms and kernel density estimations of particle kinetic energy upon impact on the blade trailing edge for 22 µm particles as percentages of emitted particles of this species.

5.3 Particle Characteristics on the Domain Outlet

As the last point we investigate the particle characteristics on the outlet boundary. Assuming a real application case in turbomachinery, this boundary would double as inlet to the next blade row in a multistage simulation and should give an

DOI: 10.13009/EUCASS2019-1022

indication of realistic assumptions for particle boundary conditions. Fig. 9 gives the total percentage of emitted particles crossing the outlet boundary, plotted over dimensionless position on the boundary face. Starting with lighter particles in Figs. 9a and 9b, a strong shading effect of the blade is visible for the RANS and time-averaged LES. In the same plots, the turbulent dispersion caused by the time-accurate LES is sufficient to remove this effect over the distance of about $3c$ downstream of the blade. These particle species are also unaffected by any initial random velocity component, indicating that their relaxation time is sufficiently low to depend only on the flow conditions inside the domain by the time they reach the outlet boundary. Heavier particles in Figs. 9c and 9d experience (multiple) reflections on the blade and cover the whole outlet boundary, retaining strong spatial coherence in the case of 44 µm particles, only somewhat weakened by unsteady turbulent effects. These species additionally exhibit significantly longer relaxation times and are still affected by the inlet random velocity component as they leave the domain. The most visible effect is shown in Fig. 9d in which all simulations collapse to a smeared distribution with the maximum shifted towards positive y-direction compared to the cases without initial random velocity component.

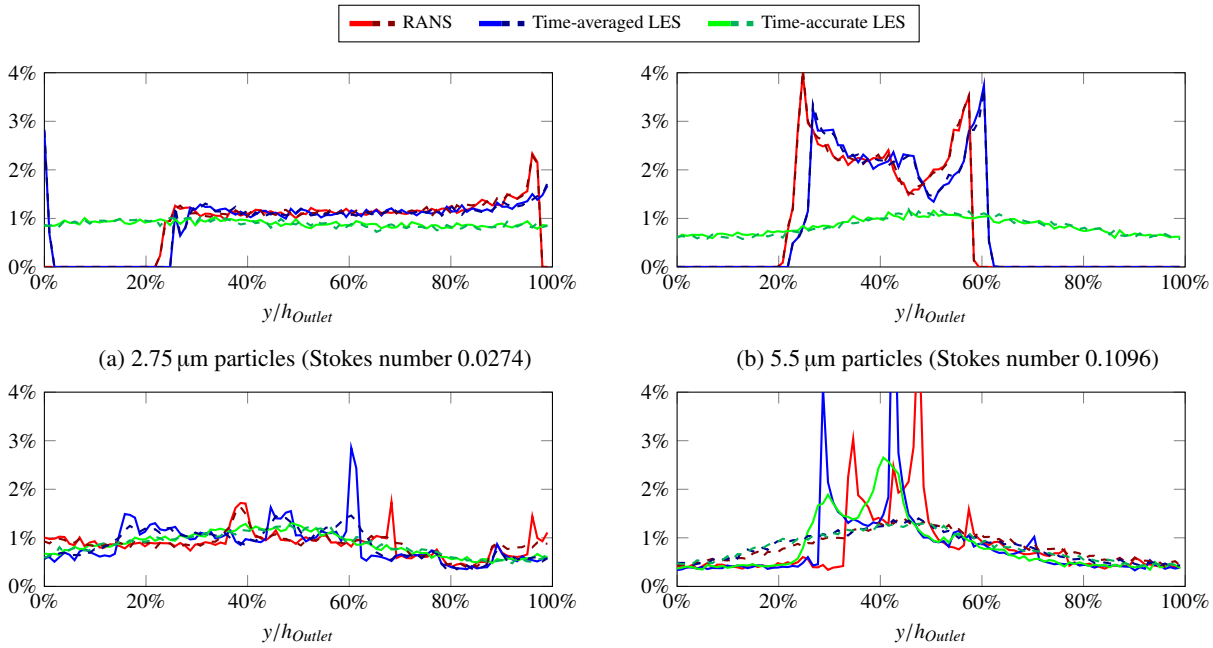

(a) 2.75 µm particles (Stokes number 0.0274)

(b) 5.5 µm particles (Stokes number 0.1096)

(c) 22 µm particles (Stokes number 1.7536)

(d) 44 µm particles (Stokes number 7.0146)

Figure 9: Percentage of emitted particles of a given size crossing the outlet boundary over dimensionless position the outlet. 0% corresponds to the upper edge, 100% to the lower edge in Fig. 1. Light solid lines denote the cases without particle inflow turbulence, dark dashed lines correspond to an initial random velocity component of magnitude 4% $|\vec{u}|_2$.

6. Conclusion and Outlook

Airborne particles resulting in erosion and fouling in turbomachinery components cause an ever rising interest in life cycle performance and maintenance prediction. A high-order framework for time-accurate simulation of particle-laden flow in turbomachinery components has been developed and successfully applied to the simulation of particle behavior in a turbine linear cascade with transitional and separating flow. Within one framework, the particle-laden flow through this test case was modeled using RANS and highly resolved LES, the latter both with an a posteriori approach where particles are advanced on the time-averaged solution and a time-accurate particle tracking coupled with the fluid time step. Comparing impact locations and higher statistics, regions of interest have been identified both with regard to the Stokes number and as physical area in the domain. Additionally, the influence on the particle inflow velocity condition was quantified by contrasting simulation using only the mean flow value against the superposition of this condition with an initial random velocity component.

On the Stokes number range, particles with a Stokes number $S \approx 1$ were shown as the species benefiting most from time-accurate tracking. These particles are light enough to show meaningful dependence on the time-resolved turbulent scales while still of sufficient mass to retain their inertial characteristics. Especially the impact kinetic energy for this particle range shows an influence from the turbulent small-scale effects which are nonlinear and anisotropic. Both factors pose substantial challenges if a particle dispersion model for these particles is to be derived. While the

DOI: 10.13009/EUCASS2019-1022

superposition of the initial particle velocity with a random component showed some smearing of the impact locations, the impact kinetic energy remained remarkably unaffected.

With regard to spatial regions of interest, the trailing edge on the suction side and the wake were identified as the areas benefiting most from time-accurate particle tracking. In the former region, significant differences in impact kinetic energy were shown between the considered cases, the comparison between time-averaged and time-accurate LES further proving these disparities to be a direct effect of turbulent dispersion. Since both erosion and fouling have a strong nonlinear correlation with impact angle and energy, shortcomings on the accurate prediction of higher statistics can substantially change the expected results. The wake region is of special interest for potential future multistage simulations. A strong correlation between turbulent dispersion and particle distribution at the outlet boundary was revealed. Furthermore, it could be shown that changes in the particle inflow velocity distribution are retained through the blade passage for particles with Stokes number significantly higher than one.

In the future, we will work on several research lines simultaneously. The Lagrangian nature of the particle discretization can cause highly varying loads on a processor, thereby diminishing the excellent scaling shown for the pure Eulerian solver. We are investigating several approaches to alleviate this problem through runtime and a priori load balancing. Furthermore, we plan to evaluate the performance of existing particle distribution models and provide time-accurate higher order statistics for their improvement. Also on our agenda is particle tracking through multiple stages using a sliding mesh approach. By obtaining time-accurate coupled inflow data for fluid and particle phase, we hope to reduce uncertainties in erosion prediction and provide reliable results in early design phases.

7. Acknowledgments

The authors gratefully acknowledge the support and the computing time on "Hazel Hen" provided by the HLRS through the project "hpcdg".

References

[1] A. Beck, P. Ortwein, P. Kopper, N. Krais, D. Kempf, and C. Koch. Towards high-fidelity erosion prediction: On time-accurate particle tracking in turbomachinery. 2018. Manuscript submitted for publication.

[2] A. Lopez, W. Nicholls, M. T. Stickland, and W. M. Dempster. CFD study of jet impingement test erosion using Ansys Fluent® and OpenFOAM®. *Computer Physics Communications*, 197:88 – 95, 2015.

[3] A. Campos-Amezcua, Z. Mazur, A. Gallegos-Munoz, A. Romero-Colmenero, J. M. Riesco-Avila, and J. M. Medina-Flores. Numerical study of erosion due to solid particles in steam turbine blades. *Numerical Heat Transfer, Part A: Applications*, 53(6):667–684, 2007.

[4] A. Mansouri, S. Shirazi, and B. McLaury. Experimental and numerical investigation of the effect of viscosity and particle size on the erosion damage caused by solid particles. In *ASME 2014 4th Joint US-European Fluids Engineering Division Summer Meeting collocated with the ASME 2014 12th International Conference on Nanochannels, Microchannels, and Minichannels*. American Society of Mechanical Engineers, 2014.

[5] A. Mansouri, H. Arabnejad, S. Karimi, S. A. Shirazi, and B. S. McLaury. Improved CFD modeling and validation of erosion damage due to fine sand particles. *Wear*, 338-339:339 – 350, 2015.

[6] M. H. Carpenter and C. A. Kennedy. Fourth-order 2N-storage Runge-Kutta schemes, NASA TM-109112. *National Aeronautics and Space Administration, Langley Research Center, Hampton, VA*, 1994.

[7] A. D. Beck, T. Bolemann, D. Flad, H. Frank, G. J. Gassner, F. Hindenlang, and C.-D. Munz. High-order Discontinuous Galerkin spectral element methods for transitional and turbulent flow simulations. *International Journal for Numerical Methods in Fluids*, 76(8):522–548, 2014.

[8] A. Murrone and P. Villedieu. Numerical modeling of dispersed two-phase flows. *AerospaceLab*, (2), 2011.

[9] G. Rudinger. *Fundamentals of Gas Particle Flow*, volume 2. Elsevier, 2012.

[10] I. Vinkovic, C. Aguirre, M. Ayrault, and S. Simoëns. Large-eddy simulation of the dispersion of solid particles in a turbulent boundary layer. *Boundary-Layer Meteorology*, 121(2):283, 2006.

[11] Q. Wang and K. D. Squires. Large eddy simulation of particle-laden turbulent channel flow. *Physics of Fluids*, 8 (5):1207–1223, 1996.

DOI: 10.13009/EUCASS2019-1022

[12] R. Israel and D. E. Rosner. Use of a generalized Stokes number to determine the aerodynamic capture efficiency of non-stokesian particles from a compressible gas flow. *Aerosol Science and Technology*, 2(1):45–51, September 1982.

[13] R. A. Wessel and J. Righi. Generalized correlations for inertial impaction of particles on a circular cylinder. *Aerosol Science and Technology*, 9(1):29–60, January 1988.

[14] R. Clift, J. R. Grace, M. E. Weber, and M. F. Weber. *Bubbles, Drops, and Particles*. Academic Press, New York, 1978.

[15] P. Ortwein, S. M. Copplestone, C.-D. Munz, T. Binder, W. Reschke, and S. Fasoulas. A particle localization algorithm on unstructured curvilinear polynomial meshes. *Computer Physics Communications*, 235:63–74, 2019.

[16] J. Marty. Numerical investigations of separation-induced transition on high-lift low-pressure turbine using RANS and LES methods. *Proceedings of the Institution of Mechanical Engineers, Part A: Journal of Power and Energy*, 228(8):924–952, September 2014.

[17] K. Hillewaert and M. Galbraith. CS2 - Spanwise periodic DNS/LES of transitional turbine cascades. In *5th International Workshop on High-Order CFD Methods*, Kissimmee, Florida, January 2018.

[18] K. Hillewaert, C. C. de Wiart, and T. Arts. DNS and LES of transitional flow around a high lift turbine cascade at low Reynolds number. In *2nd International Workshop on High-Order CFD Methods*, Cologne, Germany, May 2013. von Karman Institute, Turbomachinery Department, DLR, AIAA and AFOSR.

[19] P. Spalart and S. Allmaras. A one-equation turbulence model for aerodynamic flows. In *30th Aerospace Sciences Meeting and Exhibit*. American Institute of Aeronautics and Astronautics, January 1992.

[20] T. Bolemann, A. Beck, D. Flad, H. Frank, V. Mayer, and C.-D. Munz. High-order Discontinuous Galerkin schemes for large-eddy simulations of moderate Reynolds number flows. In *IDIHOM: Industrialization of High-Order Methods-A Top-Down Approach*, pages 435–456. Springer, 2015.

[21] ISO 12103-1:2016(E). Road vehicles - test contaminants for filter evaluation. Standard, International Organization for Standardization, Geneva, CH, March 2016. Part 1: Arizona test dust.

[22] C. C. de Wiart and K. Hillewaert. A discontinuous Galerkin method for implicit les of moderate reynolds number flows. In *53rd AIAA Aerospace Sciences Meeting*, 2015.

[23] B. P. Welford. Note on a Method for Calculating Corrected Sums of Squares and Products. *Technometrics*, 4(3): 419–420, August 1962.